Supporting Information

Nanogels Designed for Cell-Free Nucleic Acid Sequestration

Yuhang Huang,[1,†] Shangyu Li,[2,†] Logan W. C. Zettle,[2] Yingshan Ma,[2] Hani E. Naguib,[1,3,4,5] and Eugenia Kumacheva[1,2,5,]*

1   Department of Chemical Engineering and Applied Chemistry, University of Toronto, 200 College Street, Toronto, Ontario M5S 3E5, Canada
2   Department of Chemistry, University of Toronto, 80 Saint George Street, Toronto, Ontario M5S 3H6, Canada
3   Department of Mechanical and Industrial Engineering, University of Toronto, 5 King's College Road, Toronto, Ontario M5S 3G8, Canada
4   Department of Materials Science and Engineering, University of Toronto, 184 College Street, Toronto, Ontario M5S 3E4, Canada
5   Institute of Biomedical Engineering, University of Toronto, 4 Taddle Creek Road, Toronto, Ontario M5S 3G9, Canada
†   These authors contributed equally.

Content

S1. Synthesis of pAETMAC-COOH polymers

Carboxylic-acid-terminated pAETMAC (pAETMAC-COOH) was synthesized via free radical polymerization using 2,2′-azo-*bis*(2-methylpropionitrile) (AIBN) as the initiator and mecarptoacetic acid (MAA) as the chain transfer agent,[1] as shown in Scheme S1. [2-(Acryloyloxy)ethyl] trimethylammonium chloride solution (AETMAC, 80% wt. in H_2O, 12.1 g, 1 eq., 50 mmol), MAA (70.0 μL, 0.1 eq., 5 mmol) and absolute ethanol (220 mL) were mixed and stirred under nitrogen atmosphere for 30 min. In a separate vial, AIBN (0.01 eq., 0.0821 g, 0.5 mmol) and absolute ethanol (7 mL) were stirred under nitrogen atmosphere until fully dissolved and added to the reaction mixture. The entire mixture was stirred and maintained at 60 °C for 16 hrs. After that, the reaction was quenched by cooling the mixture to 25 °C and exposing it to the air. Ethanol was removed under vacuum to obtain a saturated polymer solution, which was then added dropwise into hexane. The polymer precipitate in hexane was dried and re-dissolved in ethanol. The selective precipitation was repeated for 3 times and the precipitate was freeze-dried and stored in a desiccator at room temperature.
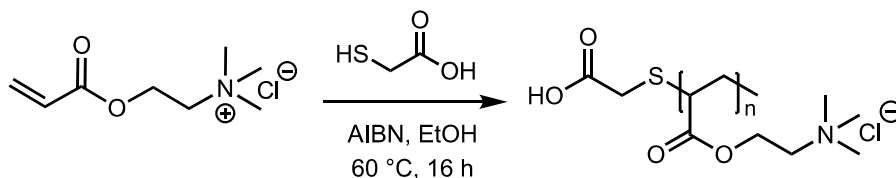

Scheme S1. Synthesis of pAETMAC-COOH *via* free radical polymerization by using AETMAC, mercaptoacetic acid, and AIBN as monomer, chain transfer agent, and initiator, respectively.

S2. Characterization of chitosan

The molecular weight of chitosan (CS) was measured by Ubbelohde-type capillary viscometry (Fisher Scientific) using five CS solutions in an acetate buffer (pH 4.5) with concentrations, c_{CS}, from 0.1 to 2.0 g/L. The intrinsic viscosity, $[\eta]$, of CS was determined by extrapolating η_{sp}/c_{CS} to zero CS concentration, shown as the slope in Figure S1. The Mark–Houwink–Sakurada equation was used to calculate the CS molecular weight, M_{CS}, as

$$[\eta] = KM_{CS}^{a} \tag{S1}$$

where K and a being constant of 0.074 and 0.76, respectively, for the acetate buffer at 22 °C.[2] Taking $[\eta] = 415$ mL/g, the molecular weight of CS was calculated to be 85 kDa.
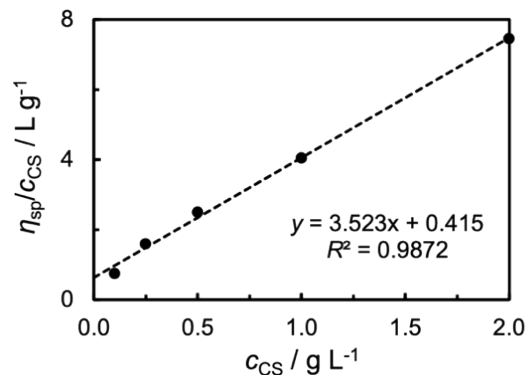
Figure S1. Variation in specific viscosity, η_{sp}, *vs.* CS solution in acetate buffer with concentration, c_{CS}. The dashed line is the linear fit with the intercept being the intrinsic viscosity, $[\eta] = 415$ mL/g.

The degree of deacetylation (DDA) of chitosan was determined by ^{1}H NMR spectroscopy (D$_2$O, 4% v/v DCl, 500 MHz, 20 °C) as[3]

$$DDA = \left(1 - \frac{\frac{A_{H(1.94)}}{3}}{\frac{A_{H(2.9-4.5)}}{7}}\right) \times 100\% \tag{S2}$$

where $A_{H(1.94)}$ is the area of the *N*-acetyl protons and $A_{H(2.9-4.5)}$ is the area of the protons on D-glucose rings. Taking $A_{H(1.94)} = 1.00$ and $A_{H(2.9-4.5)} = 10.02$, the DDA value was determined to be 77%.

The mass of the CS monomer unit was estimated from DDA as $m_0 = 161 + 42(1-DDA) = 171$ g/mol. The number of D-glucose rings (that is, the degree of polymerization) of CS was determined as $M_{CS}/m_0 = 500$. Based on the degree of polymerization and the DDA of CS, the number of amine groups was determined as 385 per CS molecule.

S3. Synthesis of CS-*g*-pAETMAC copolymers

The grafting of pAETMAC onto chitosan (CS) backbone was achieved via *N*-ethyl-*N'*-(3-(dimethylamino)propyl)carbodiimide/*N*-hydroxysuccinimide (EDC/NHS)-mediated coupling, as shown in Scheme 2. Chitosan was stirred in 2-(*N*-morpholino)ethanesulfonic acid (MES) buffer (0.1 M, pH 5) for 30 min. In a vial, pAETMAC, EDC, and NHS were dissolved in MES buffer (0.1 M, pH 5) and added into the chitosan solution. The reaction mixture was stirred overnight. The non-grafted pAETMAC and reagents other than the desired product were removed by dialysis (cellulose membrane, 12 kDa MWCO cut-off, Sigma–Aldrich) against deionized water for 7 days, with water being changed every day. The copolymer was freeze-dried and stored in a desiccator at room temperature. Various feeding ratios of reagents and reaction temperatures were used for the synthesis of the graft copolymer CS-*g*-pAETMAC with different grafting degree, $\sigma_{pAETMAC}$, as shown in Table S1.
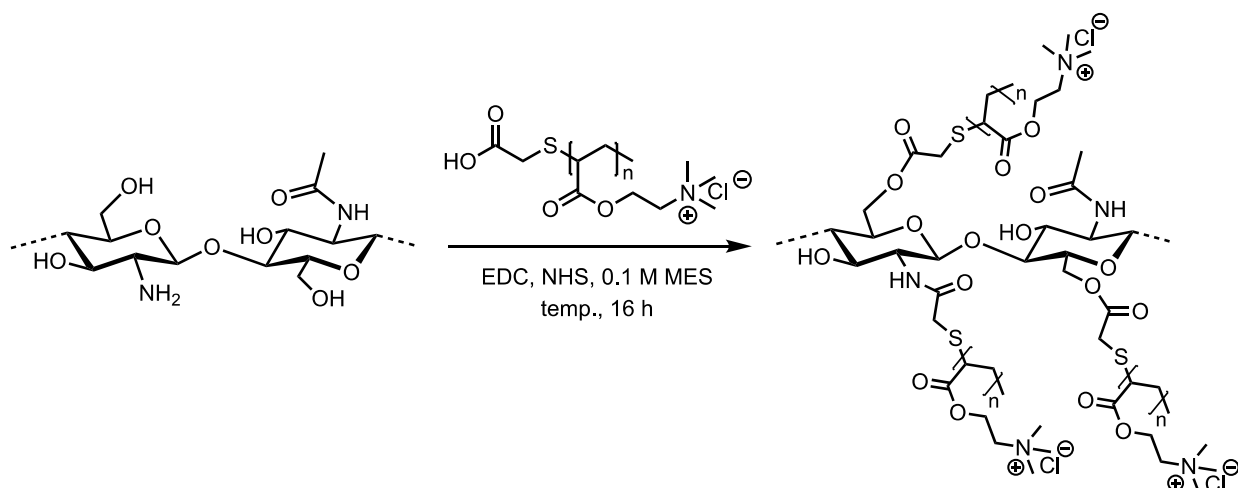
Scheme S2. Grafting of pAETMAC onto CS backbone, achieved via EDC/NHS-mediated coupling.

Table S1. Recipes for the synthesis of CS-*g*-pAETMAC at varying $\sigma_{pAETMAC}$.

$m_{pAETMAC}$ mg	m_{CS} mg	m_{EDC} mg	m_{NHS} mg	V_{MES} mL	T °C	$\sigma_{pAETMAC}$
4.5 (100 eq., 2 μmol)	1.7 (1 eq., 0.0200 μmol)	70 (300 eq., 0.60 μmol)	115 (300 eq., 0.6 μmol)	10	25	36
840 (208 eq., 0.37 mmol)	151 (1 eq., 1.7765 μmol)	180 (878 eq., 1.56 mmol)	299 (878 eq., 1.56 mmol)	15	40	103
1615 (417 eq., 0.71 mmol)	145 (1 eq., 1.7059 μmol)	245 (1248 eq., 2.13 mmol)	408 (1248 eq., 2.13 mmol)	30	25	254
1938 (2071 eq., 0.85 mmol)	35 (1 eq., 0.4118 μmol)	293 (6192 eq., 2.55 mmol)	489 (6192 eq., 2.55 mmol)	30	40	570

We note that EDC–NHS chemistry is typically used for the coupling between carboxylic acids and amines by forming amide bonds. Through the coupling mechanism (shown in Scheme S3), the carboxyl-acid end-groups of pAETMAC chains react with EDC to form reactive *o*-acylisourea esters, followed by the formation of semi-stable NHS-esters. Next, the nucleophiles (e.g., primary amines) conjugate via nucleophilic addition to the carbonyls in the NHS-esters to form amide bonds. Chitosan, however, contains two types of nucleophiles in its backbone, that is, C_2-amino and C_6-hydroxyl groups. In the grafting reaction of carboxylic-acid-terminated pAETMAC to CS, the nucleophilicity of C_2-amino groups is stronger than that of C_6-hydroxyl groups,[4–7] and thus, the coupling would primarily occur between the carboxyl groups on pAETMAC and amino groups on CS. Nevertheless, as the C_6-hydroxyl groups on the CS were not protected, they could also couple with pAETMAC-COOH via esterification.[4–7] Such dual coupling of pAETMAC-COOH with the C_2-amino and C_6-hydroxyl groups of CS explains the fact that, as the feeding ratio of pAETMAC-COOH to CS increased, the values of $\sigma_{pAETMAC}$ exceeded the number of amino groups per CS molecule.
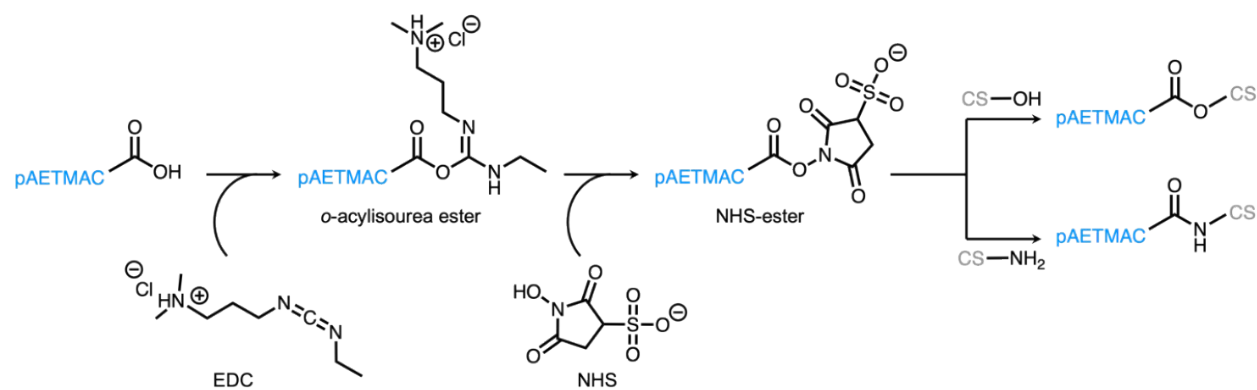
Scheme S3. Mechanism of EDC–NHS coupling.

## S4. Characterization of pAETMAC-COOH and CS-*g*-pAETMAC

The structure of CS, pAETMAC-COOH and CS-*g*-pAETMAC with various grafting degree was characterized by ATR FT-IR (Figure S2). The spectrum of CS molecules exhibited absorption at 3300 (broad, N–H & O–H stretch), 2970 (Csp^3–H stretch), 1641 (amide C=O stretch), and 1533 cm^{-1} (amide N–H bending). In addition, a distinct band at 1100 cm^{-1} (the region shaded in grey) corresponded to the C–O stretch of aliphatic ether in the D-glucose ring of CS. In the spectrum of pAETMAC, a broad band at 3360 cm^{-1} corresponded to O–H stretch in the carboxylic-acid end groups, while the bands at 1728 and 1159 cm^{-1} (the regions shaded in blue) correspond to the ester C=O and C–O stretch in the pAETMEC repeat units, respectively. Upon cross-linking between pAETMAC-COOH and CS, the resulting CS-*g*-pAETMAC copolymer exhibited characteristic bands of both reagents (that is, grey and blue boxes), which corroborates the functionalization of CS backbone by pAETMAC grafting.

Figures S3–S5 show the ^{1}H NMR spectra of CS, pAETMAC-COOH and CS-*g*-AETMAC. In the NMR spectrum of CS, the peaks ranging from 2.5–4.1 ppm correspond to the D-glucose ring protons, while the small peak at 4.6 ppm correspond to the anomeric protons. The sharp peak at 2.1 ppm correspond to the methyl groups in both the acetylated repeat units of CS and acetic acid-d_4 (solvent). The NMR spectrum of pAETMAC exhibited peaks at 4.6, 3.8, 3.3, 2.6 and 1.9 ppm, corresponding to the ester methylene, amine methylene, amine methyls, *α*-methine and *β*-methyl.[8,9] The NMR spectrum of CS-*g*-AETMAC showed similar resonance compared to the spectrum of pAETMAC, the peaks originating from CS and pAETMAC overlapped in the 3.0–4.0 and 1.6–2.2 ppm regions.
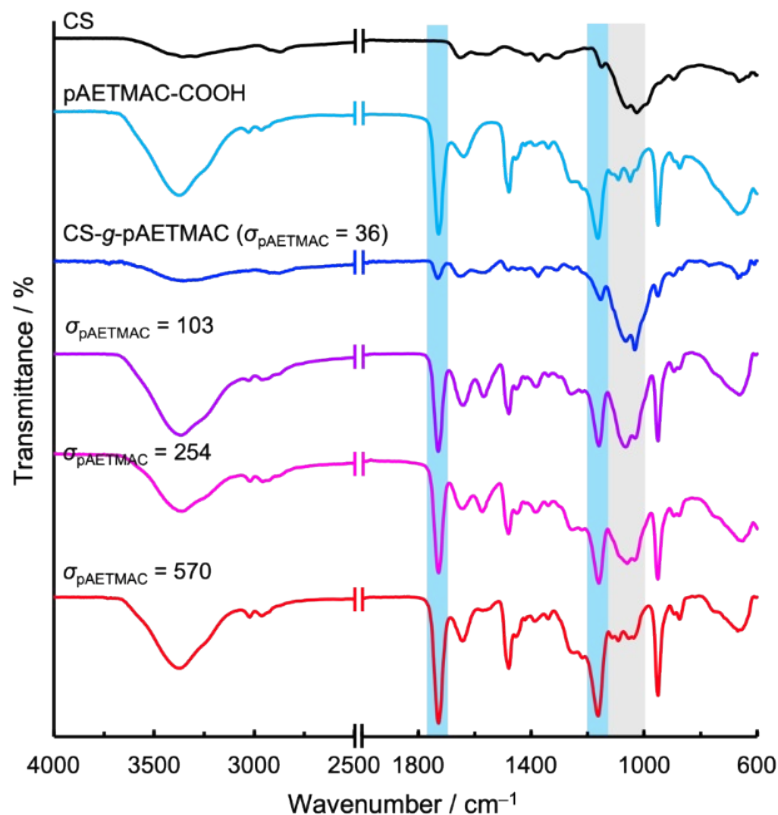
Figure S2. ATR FT-IR spectrum of CS, pAETMAC-COOH, and CS-*g*-pAETMAC with various $\sigma_{pAETMAC}$. Blue and grey boxes indicate characteristic bands of pAETMAC and CS molecules, respectively.
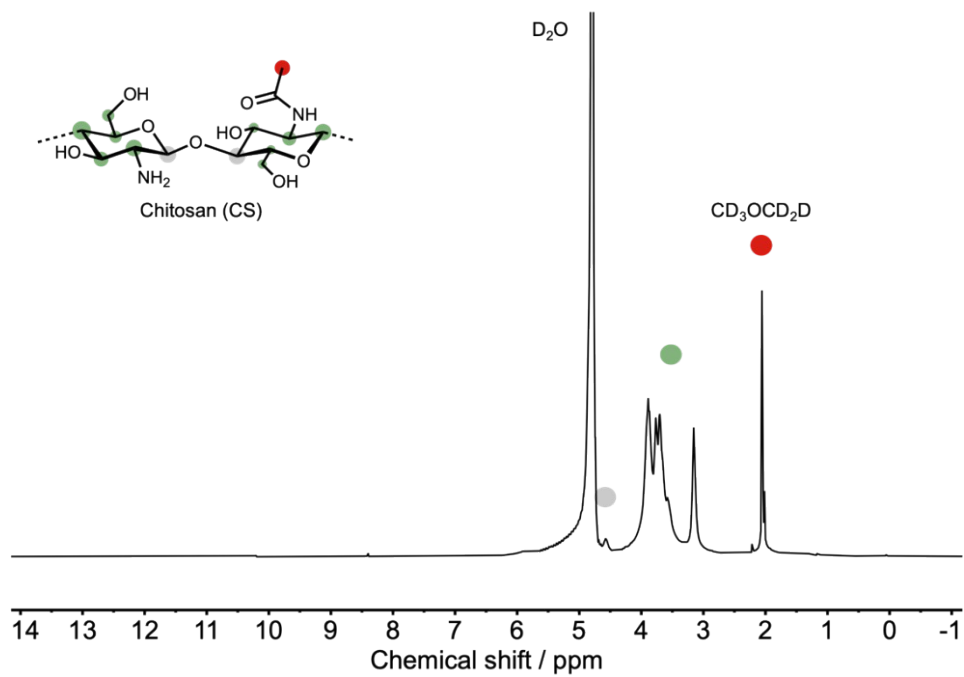
Figure S3. ^{1}H NMR (500 MHz) spectrum of CS in D_2O with 1 wt% CD_3CO_2D-d_4.
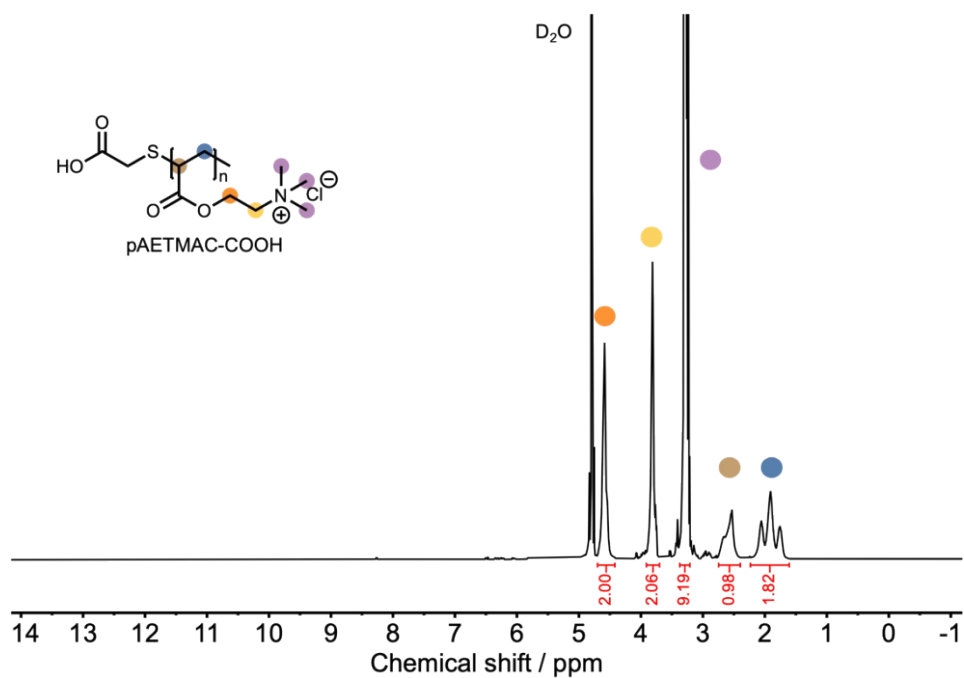
Figure S4. ^{1}H NMR (500 MHz) spectrum of pAETMAC-COOH in D_2O.
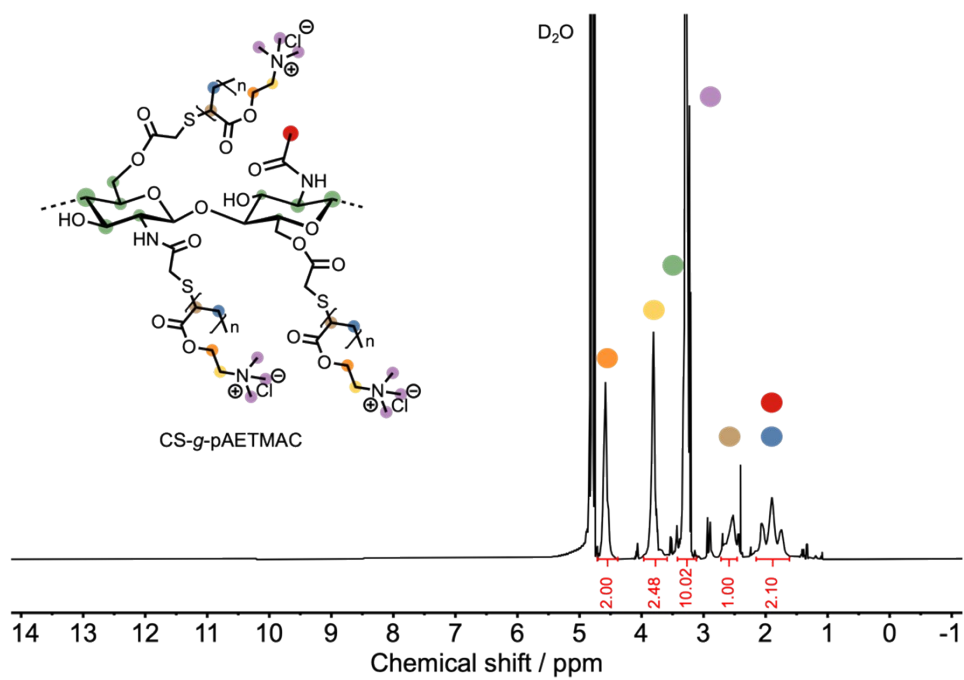

Figure S5. ^{1}H NMR (500 MHz) spectrum of CS-*g*-pAETMAC in D_2O.

S5. End-group titration of pAETMAC-COOH

In addition to gel permeation chromatography, the number-average molecular weight, M_n, of the pAETMAC-COOH polymers was determined by titrating the carboxylic-acid end-groups. The polymer (60 mg) was dissolved in deionized water (5 mL) and stirred overnight. The polymer solution was then titrated with 0.01 M NaOH, with pH monitored by a pH meter (EcoMat P25). The molecular weight M_n was calculated as

$$M_n = \frac{m_{pAETMAC}}{c_{NaOH}V_{NaOH}} \tag{S3}$$

where $m_{pAETMAC}$ is the mass of the polymer, c_{NaOH} is the molar concentration of NaOH, and V_{NaOH} is the volume of NaOH consumed when pH inflection of the polymer solution occurred (Figure S6). The end-group titration gave an average M_n of 2060 g/mol, similar to that determined by gel permeation chromatography.
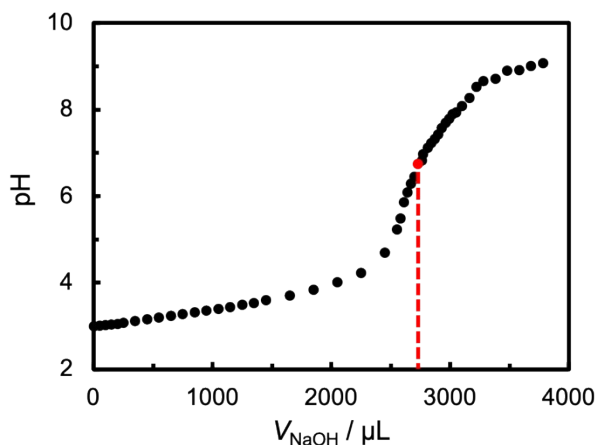
Figure S6. Titration curve of aqueous solution of pAETMAC-COOH by 0.01 M NaOH. Red dot indicates the addition volume of NaOH (2.272 mL) when pH inflection occurred.

S6. Nanogel preparation

The nanogels were prepared by adding 200 μL of an aqueous solution of sodium triphosphate (TPP) into 2 mL of CS-*g*-pAETMAC solution. The concentration ratio between the TPP, c_{TPP}, and the CS content, c_{CS}, in the nanogel dispersion was 0.01, with the latter calculated as[1]

$$c_{CS} = m_{CS-g-pAETMAC}\left(\frac{M_{CS}}{M_{CS} + \sigma_{pAETMAC}M_{pAETMAC}}\right) \tag{S4}$$

where $m_{CS-g-pAETMAC}$ is the mass of CS-*g*-pAETMAC, M_{CS} and $M_{pAETMAC}$ are the molar mass of CS (determined to be 85 kDa) and pAETMAC (2.1 kDa), respectively, and $\sigma_{pAETMAC}$ is the grafting

degree of pAETMAC per CS molecule. The recipes of used for the preparation of nanogels with different $\sigma_{pAETMAC}$ are shown in Table S2.

Table S2. Recipes for the preparation of cNGs at varying $\sigma_{pAETMAC}$

cNGs	$\sigma_{pAETMAC}$	$c_{CS\text{-}g\text{-}pAETMAC}$ mg mL^{-1}	c_{CS} mg mL^{-1}	c_{TPP} μg mL^{-1}
CNG$_{36}$	36	10.0	5.12	51.2
CNG$_{103}$	103	10.0	2.68	26.8
CNG$_{570}$	570	10.0	0.62	6.21

S7. Polydispersity index of nanogels

The polydispersity index of the nanogels was measured by dynamic light scattering (Figure S7a). At pH of 3.0 and 7.4, the CS nanogels ($\sigma_{pAETMAC} = 0$) had polydispersity of ~0.3 and ~0.8, respectively. The increase in polydispersity these nanogels at higher pH was caused by the deprotonation of amino groups on the CS backbones, resulting in their weaker ionic crosslinking and thus, reduced colloidal stability. In contrast, the cNG nanoparticles did not exhibit a significant change in polydispersity at elevated pH, due to the substitution of amino groups of the CS by the grafted pAETMAC chains with quaternary ammonium groups with $pK_a = 35$.[10]
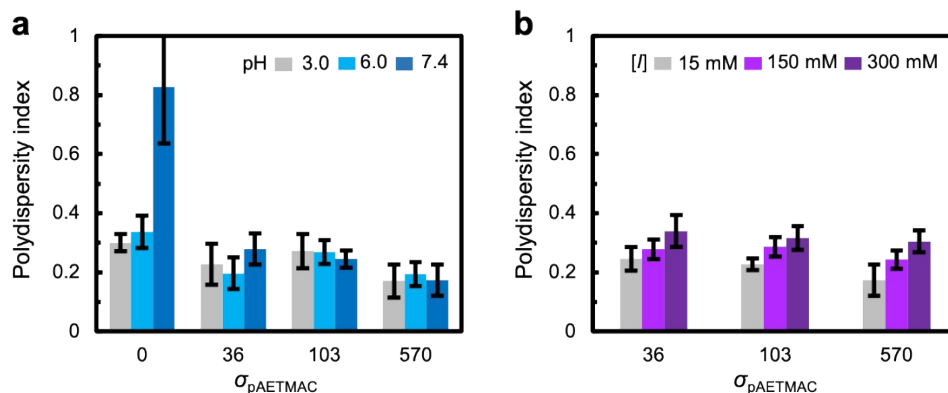
Figure S7. Polydispersity index of cNGs at (a) varying $\sigma_{pAETMAC}$ and pH in 15 mM PBS buffer and (b) at varying $\sigma_{pAETMAC}$ and ionic strength in PBS buffer.

The effect of ionic strength, $[I]$, on the polydispersity of the cNGs is shown in Figure S7b. At pH = 7.4, the polydispersity index of cNGs exhibited slight increase with $[I]$ increasing from 15 to 300 mM, which was due to the screening of the electrostatic interactions and thus weaker cross-linking of the CS-g-pAETMAC copolymers.

S8. Colloidal stability of nanogels

A 0.1 wt% nanogel dispersion in 150 mM PBS buffer was stored at room temperature (22 °C) for 14 days, and the colloidal stability of the nanogels was monitored by changes of extinction of the dispersion at λ = 600 nm, using a Vairan Cary 50 UV–Vis spectrometer. The extinction was normalized by dividing it by extinction of the nanogel dispersion on day 0. As shown in Figure S8, the dispersion of the dispersion of nanogel with grafting degrees $\sigma_{pAETMAC}$ of 570 and 103 exhibited colloidal stability after 14-day storage, as no significant change of extinction (< 10%) was observed. The nanogel with grafting degree $\sigma_{pAETMAC}$ of 36 exhibited >10% increase in extinction, indicating its insufficient colloidal stability, which was attributed to the relatively weak surface charge (ξ-potential ~ 10 mV).
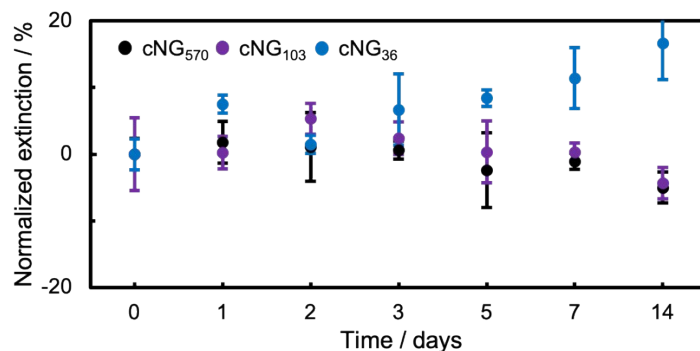
Figure S8. Normalized extinction of the dispersion of nanogels with various $\sigma_{pAETMAC}$.

S9. Diffusion-ordered NMR spectroscopy

Figure S9 shows the ^{1}H NMR spectrum of dextran molecules with an average molar mass of 40 kDa in D_2O. The peak at 4.99 ppm corresponds to the anomeric proton of the dextran molecules,[11] which was chosen for the resonance attenuation fitting in DOSY experiments.
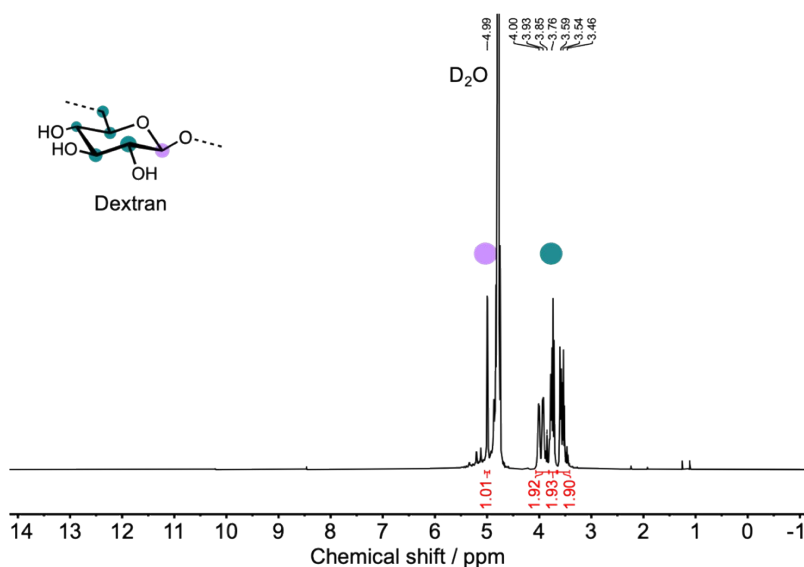

Figure S9. ^{1}H NMR (500 MHz) spectrum of dextran in D_2O.

The DOSY experiments were conducted on an Oxford DD2-500 Hz spectrometer with a OneNMR Direct Detect Probe with a ^1H 90° pulse width of 8.4 μs. Longitudinal (T_1) relaxation of the cNG dispersions and the dextran solutions was determined prior to DOSY measurements. The recycle delays of DOSY measurements were set to be 5-fold of the longest T_1. The length of the gradient, δ, and the diffusion time, Δ, were set to 3.5 and 300.0 ms, respectively. An array of spectra was collected with varying gradient strength, g, from 1.8 to 45.0 G/cm in 15 increments to yield ~90% attenuation of the dextran signals. All the spectra were obtained using 32 scans per gradient strength, 2.0 s relaxation delay, 10.0 s acquisition time, and 4006.4 Hz spectral window centred around the D_2O signal. The intensity of attenuated signals was fitted into the following equation[12]

$$\frac{I}{I_0} = exp\left[-D\gamma^2\delta^2g^2\left(\Delta - \frac{\delta}{3}\right) \right]$$
(S5)

where I_0 and I are the intensities of the dextran signal (4.99 ppm) at the lowest gradient strength $g_0 = 1.8$ G/cm and at varying gradients g, γ is the gyromagnetic ratio of ^1H (42.58 MHz/T), and D is a fitting parameter which equals to the diffusion coefficient of the dextran.

The representative ^1H NMR spectra for the attenuation of the resonances for the dextran molecules encapsulated in cNG$_{570}$ and the free dextran molecules in the 150 mM PBS buffer (D_2O) are shown in Figure S10 and S11, respectively.
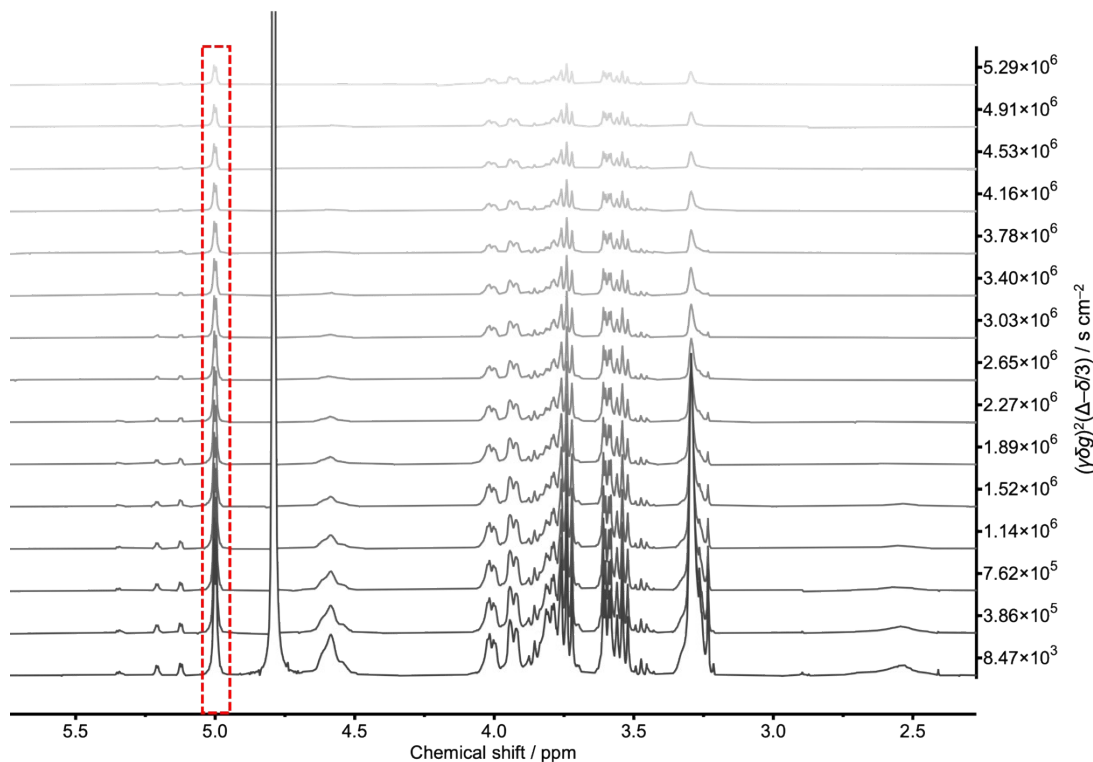
Figure S10. ^1H NMR spectra of dextran encapsulated in cNG$_{570}$ at varying gradient strength. The red box shows the peaks used for the resonance attenuation fitting.
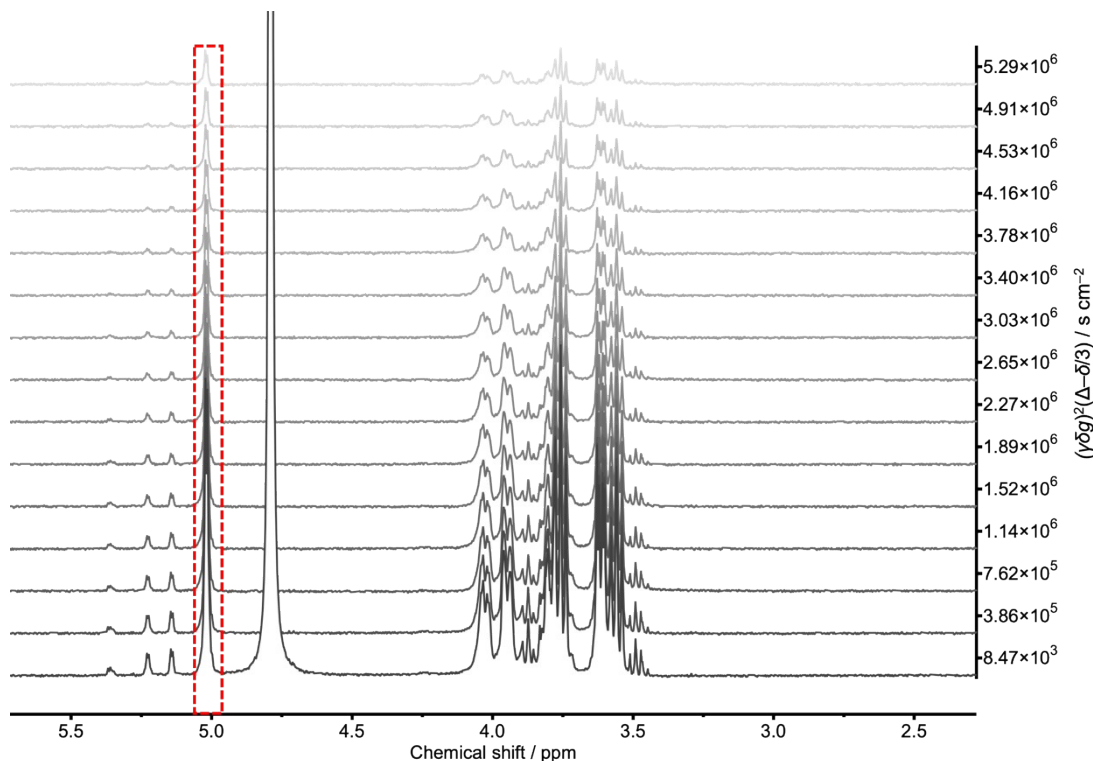
Figure S11. ^{1}H NMR spectra of dextran in 150 mM PBS buffer at varying gradient strength g. The red box shows the peaks used for the resonance attenuation fitting.

The pulse-field gradient signal decays I/I_0 for dextran in cNG$_{570}$ and in 150 mM PBS buffer were plotted against $(\gamma\delta g)^2(\Delta-\delta/3)$, as shown in Figure 2 (main text), and the diffusion coefficients of dextran molecules in the nanogels and in the buffer were extrapolated from the plots as $D = 3.18\times10^{-11}$ m^2/s and $D_0 = 3.86\times10^{-11}$ m^2/s, respectively. Since the hydrodynamic radius of dextran (5 mg/mL) in 150 mM PBS buffer was measured to be $r_d = 7$ nm by dynamic light scattering (Figure S12), the mesh size of cNG$_{570}$ in 150 mM PBS buffer was estimated by the hydrodynamic diffusion model (eq. 1, main text) to be 37 nm.
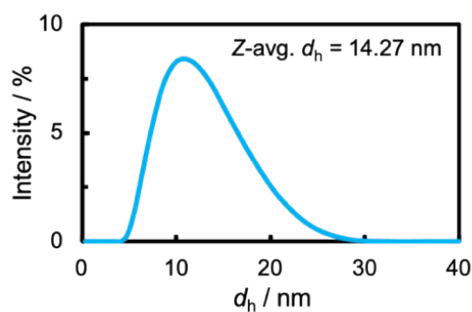
Figure S12. Intensity-weighted CONTIN distribution of dextran in in 150 mM PBS buffer.

Similarly, the mesh sizes of cNGs with varioug compositions in different buffers were determiend by (i) conducting DOSY measurements for dextran in the nanogel and in the buffer, (ii) extrapolating diffusion coefficients D and D_0 from the corresponding NMR signal decays, (iii) determining hydrodynamic radius of the dextran, and (iv) using the hydrodynamic diffusion

model. Figure S13 shows the NMR signal decays for dextran in cNGs with varying grafting degree σ_{pAETMAC} in 150 mM PBS buffer, with extrapolated diffusion coefficients and hydrodynamic radius of dextran (shown in Table S3).
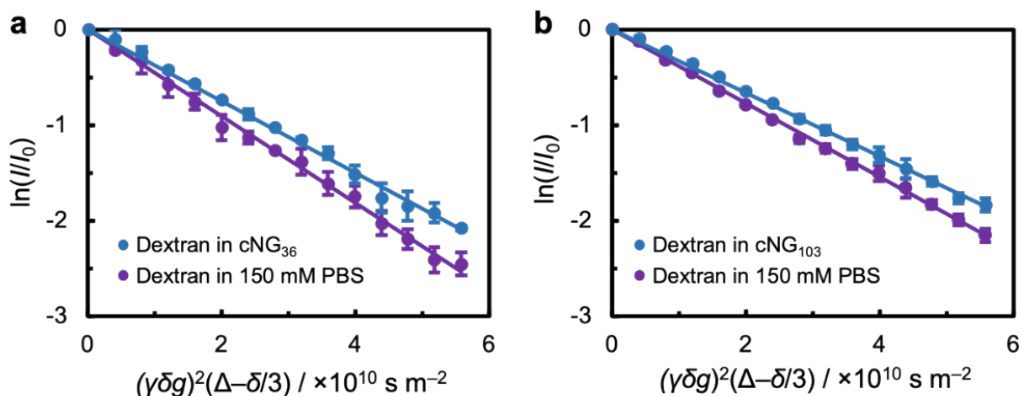
Figure S13. Pulse-field gradient NMR signal decay plots of dextran in (a) cNG$_{36}$ and (b) cNG$_{103}$ in 150 mM PBS buffer. Lines are linear fits to the experimental data.

Table S3. Diffusion coefficients and hydrodynamic radius of dextran in the nanogel at varying grafting degree σ_{pAETMAC} in 150 mM PBS buffer.

cNGs	σ_{pAETMAC}	D_0 / $\times 10^{-11}$ m^2 s^{-1}	d_{d} / nm	D / $\times 10^{-11}$ m^2 s^{-1}
CNG$_{36}$	36	3.86 ± 0.03	14.27 ± 4.52	3.38 ± 0.32
CNG$_{103}$	103	3.86 ± 0.03	14.27 ± 4.52	3.31 ± 0.29
CNG$_{570}$	570	3.86 ± 0.03	14.27 ± 4.52	3.18 ± 0.25

Figure S14 shows the NMR signal decays for dextran in cNG$_{570}$ in 150 mM PBS buffer at varying pH, with extrapolated diffusion coefficients and hydrodynamic radius of dextran (shown in Table S4).
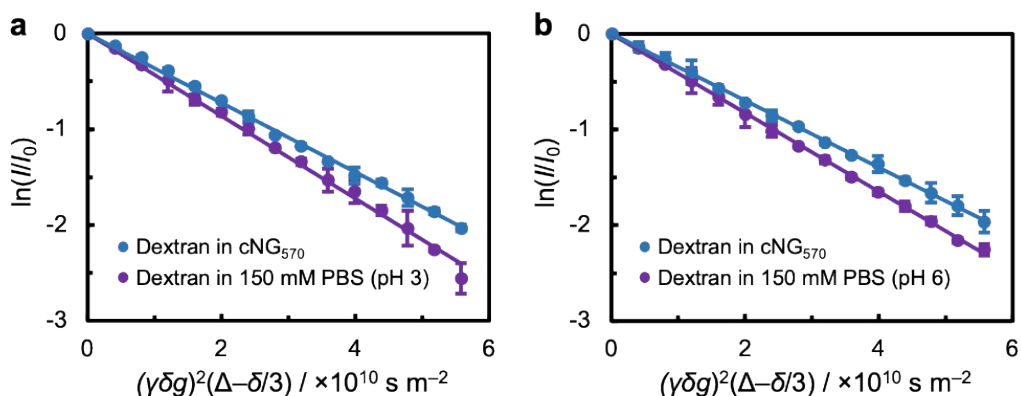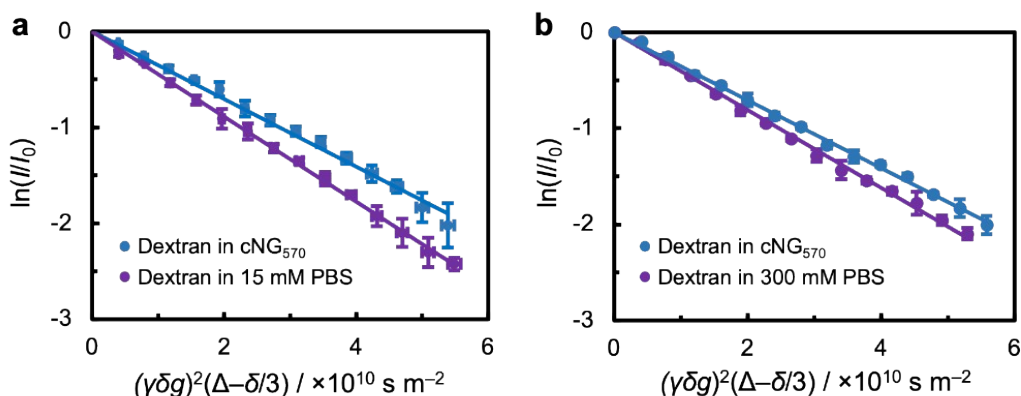

Figure S14. Pulse-field gradient NMR signal decay plots of dextran in cNG$_{570}$ in 150 mM PBS buffer at (a) pH = 3 and (b) pH = 6. Lines are linear fits to the experimental data.

Table S4. Diffusion coefficients and hydrodynamic radius of dextran in cNG$_{570}$ in 150 mM PBS buffer at varying pH

pH	D_0 / $\times 10^{-11}$ m^2 s^{-1}	d_d / nm	D / $\times 10^{-11}$ m^2 s^{-1}
3.0	4.30 ± 0.41	14.57 ± 2.97	3.62 ± 0.28
6.0	4.11 ± 0.04	13.23 ± 2.28	3.49 ± 0.25
7.4	3.86 ± 0.03	14.27 ± 4.52	3.18 ± 0.25

Figure S15 shows the NMR signal decays for dextran in cNG$_{570}$ in PBS buffer at varying ionic strength [I], with extrapolated diffusion coefficients and hydrodynamic radius of dextran (shown in Table S5).

Figure S15. Pulse-field gradient NMR signal decay plots of dextran in cNG$_{570}$ in PBS buffer at (a) [I] = 150 mM and (b) [I] = 300 mM. Lines are linear fits to the experimental data.

Table S5. Diffusion coefficients and hydrodynamic radius of dextran in cNG$_{570}$ in PBS buffer at varying ionic strength.

[I] / mM	D_0 / $\times 10^{-11}$ m^2 s^{-1}	d_d / nm	D / $\times 10^{-11}$ m^2 s^{-1}
15	4.44 ± 0.12	12.53 ± 0.64	3.53 ± 0.28
150	3.86 ± 0.03	14.27 ± 4.52	3.18 ± 0.25
300	3.74 ± 0.50	14.40 ± 4.36	3.14 ± 0.28

S10. Nanogel size and size distribution as function of ionic strength

The hydrodynamic size and size distribution profiles of the cNG_{570} dispersion were measured at increasing ionic strength, $[I]$. As shown in Figure S16, the nanogel size weakly increased from 380 to 480 nm when $[I]$ increased from 15 to 300 mM, respectively. Following the increase in ionic strength, the electrostatic screening effect led to a weaker crosslinking between CS-g-pAETMAC chains. The resulting gel swelling could result in the simultaneous increase of gel's mesh size and dimensions. We note that, however the ~15% increase in the hydrodynamic diameter of cNG_{570} was less significant than a two-fold increase in the nanogel mesh size. A weak increase in cNG_{570} dimensions could be caused by the loss of material from the surface of this physically crosslinked nanogel at elevated $[I]$.

The dissociation of the nanogels is evidenced from their size distribution profiles (Figure S16); the polydispersity index of the nanogels increased from 0.16 to 0.34 when $[I]$ increased from 15 to 300 mM. We note that, with $[I]$ increasing further from 300 mM to 1 M, the hydrodynamic size of cNG_{570} dramatically decreased to 76 nm. Thus, we conclude that screening of the nanogel charges at a high $[I]$ and weakened ionic cross-linking caused the nanogel dissociation. As a result, the competition between partial material loss and gel swelling with increasing $[I]$ caused the nonlinear dependence between the change in of nanogel size and mesh size.
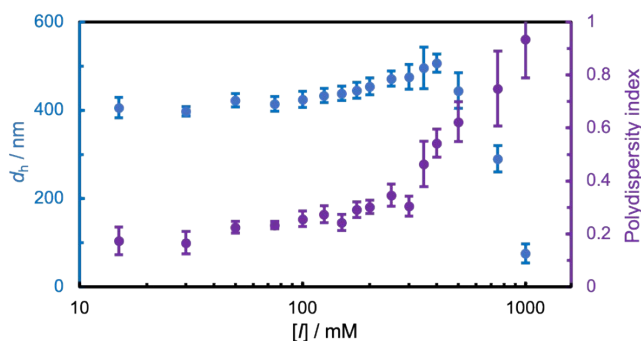
Figure S16. Hydrodynamic size (d_h) and size distribution (polydispersity index) of cNG_{570} at varying ionic strength ($[I]$).

S11. Determination of charge density of nanogels

The surface charge density, σ_c, of the cNGs was determined using their effective hydrodynamic diameters, d_h, and ζ-potentials as[13]

$$\sigma_c = \epsilon \xi r_D^{-1} \left(1 + \frac{2}{d_h r_D^{-1}}\right) \tag{S6}$$

where ε is the electrical permittivity of water (7.1×10^{-10} C/Vm) and r_D is the Debye length, which is estimated from the solvent ionic strength, $[I]$: $r_D^{-1} = \dfrac{0.304}{\sqrt{I}}$.[13] Table S6 summarizes the values of charge density of cNGs with various $\sigma_{pAETMAC}$ in various buffer conditions.

Table S6. Charge density of cNGs with various $\sigma_{pAETMAC}$ and under various buffer condition.

cNGs	$[I]$ / mM	d_h / nm	ζ-potential / mV	σ_c / mC m^{-2}
	15	260.1	9.7	46.5
CNG$_{36}$	150	298.0	5.2	3.9
	300	303.3	2.2	0.1
	15	347.9	26.9	47.6
CNG$_{103}$	150	350.8	19.5	11.0
	300	385.0	11.5	4.6
	15	405.8	35.7	63.1
CNG$_{570}$	150	438.6	28.2	15.8
	300	480.9	16.9	6.70

## S12. Characterization of DNA molecules

Four types of DNA molecules, including oligodeoxynucleotide ODN1826, genomic DNA extracted from salmon testes, and calf thymus, were used for sequestration experiments. The hydrodynamic diameter, d_{DNA}, and ζ-potential of the DNA molecules (~0.1 mg/mL, 150 mM PBS buffer) were measured on a Malvern Zetasizer Nano ZS-ZEN3600 at 25 °C (Table S7). The charge densities σ_c of the DNA molecules was determined using their dimensions and ζ-potentials (eq. S4).

Table S7. Physicochemical properties of DNA molecules.

DNA	M_w / kDa	d_{DNA} / nm	ζ-potential / mV	σ_c / mC m^{-2}	Ref
ODN1826	0.7	11.0	−22.5	18.4	14
Herring sperm	13.5	23.2	−30.9	19.1	15
Salmon testes	~1300	121.9	−32.6	18.6	16
Calf thymus	~8200	208.2	−35.7	20.2	17

## S13. Fluorescence intensity–concentration calibration of DNA–GelRed complex

Fluorescent dye GelRed intercalates nucleic acid and exhibits emission in PBS buffer at 600 nm under excitation at 520 nm. The photoluminescence (PL) intensity of the DNA–GelRed was measured for the determination DNA sequestration efficiency of cNGs (i.e., the fraction of unbound DNA molecules by cNGs). Figure S17a–c show the excitation and emission spectra of the GelRed bound to calf thymus DNA, salmon testes DNA, and ODN1826 (cfDNA) molecules, respectively. Calibration graphs for three types of DNA molecules were constructed by measuring the PL intensity of the DNA–GelRed solutions with DNA concentrations from 6.3×10^{-2} to 1 μM. Figure S17d–f show the linear increase of PL intensity with the concentration of calf thymus DNA, salmon testes DNA, and ODN1826 molecules, respectively, along with the correlation coefficients, R^2, for the linear fits.
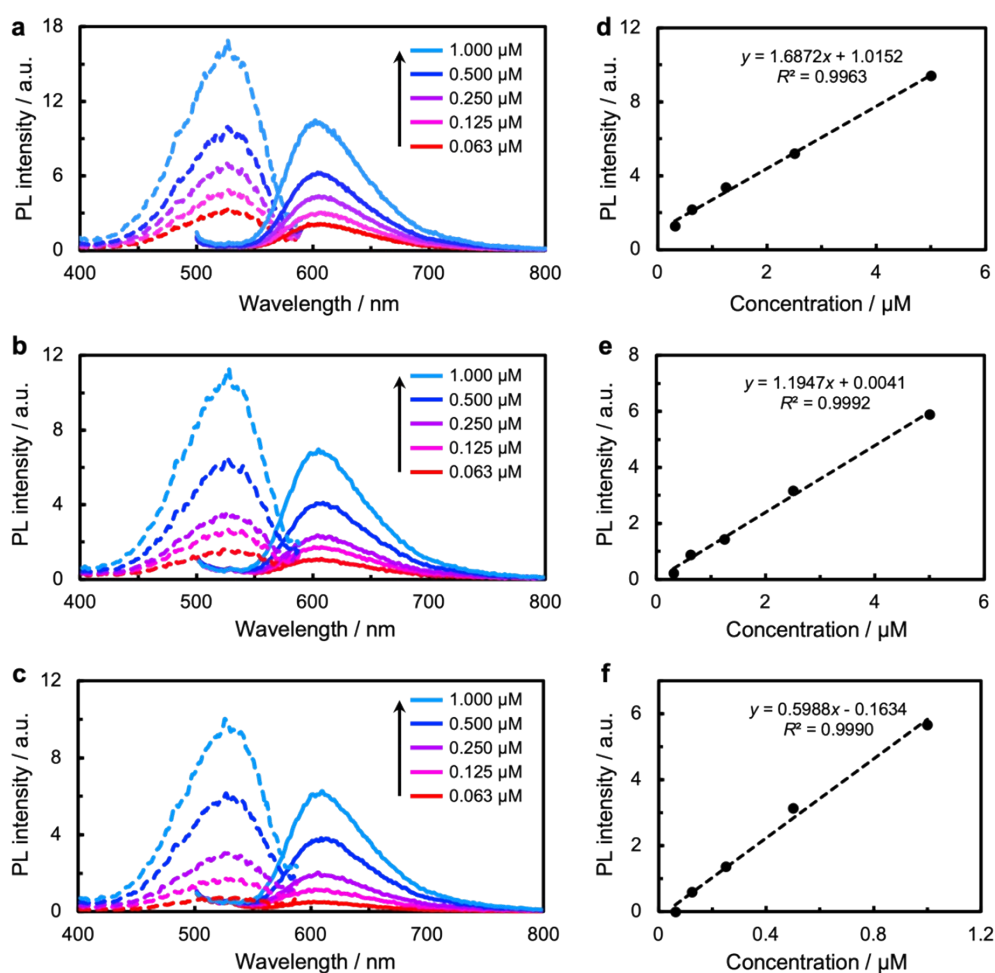
Figure S17. Photoluminescence intensity–concentration calibration graphs of the GelRed–DNA complex. (a–c) Excitation and emission spectra of GelRed bound to calf thymus DNA, salmon testes DNA, and ODN1826 (cfDNA) molecules, respectively. (b–f) Calibration graphs showing linear increase in photoluminescence intensity with the concentration of calf thymus DNA, salmon testes DNA, and ODN1826 (cfDNA) molecules, respectively.

S14. CONTIN size distribution of DNA–cNG$_{570}$ complex

Figure S18a shows the CONTIN size distributions of DNA molecules from calf thymus, cNG$_{570}$, and the complex formed by calf thymus DNA and cNG$_{570}$, determined by dynamic light scattering. The scattering peak intensity of calf thymus DNA at ~200 nm was largely preserved after complex formation, indicating that most of the calf thymus DNA remained unattached to cNGs. Such limited DNA uptake was ascribed to the hindrance of the diffusion of DNA molecules in the nanogel. For DNA molecules from salmon testes and cfDNA molecules (Figure S18b and c, respectively), the peak intensity of the DNA molecules significantly reduced after complex formation, indicating that DNA molecules were bound to the cNGs. The enhanced sequestration was attributed to the reducing size ratio of DNA-to-gel mesh d_{DNA}/Ξ, which allowed DNA binding on the surface and in the interior of the cNGs.
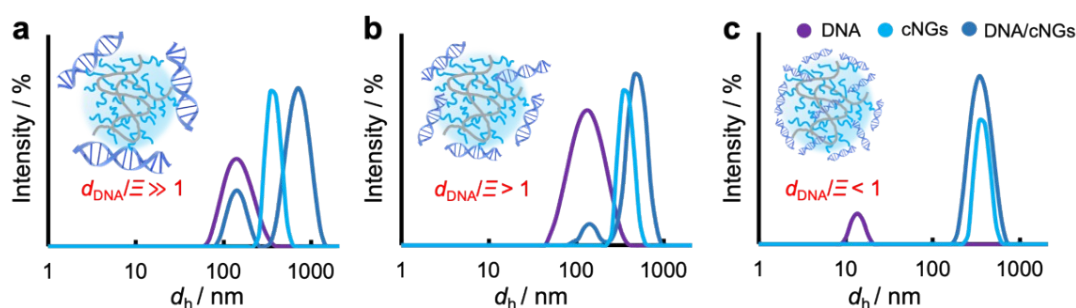
Figure S18. Size distribution of complexes formed by cNG$_{570}$ and (a) calf thymus DNA, (b) salmon testes DNA, or (c) ODN1826 (cfDNA). Size distribution of the DNA molecules and cNG$_{570}$ alone are also shown in comparison.

References

1. Huang, Y.; Morozova, S. M.; Li, T.; Li, S.; Naguib, H.E.; Kumacheva, E. Stimulus-responsive transport properties of nanocolloidal hydrogels. *Biomacromolecules* **2022**, *24*, 1173-1183.
2. Rinaudo, M.; Milas, M.; Le Dung, P. Characterization of chitosan. Influence of ionic strength and degree of acetylation on chain expansion. *Int. J. Biol. Macromol.* **1993**, *15*, 281-285.
3. Pérez-Álvarez, L.; Ruiz-Rubio, L.; Vilas-Vilela, J.L. Determining the deacetylation degree of chitosan: Opportunities to learn instrumental techniques. *J. Chem. Edu.* **2018**, *95*, 1022-1028.
4. Tomihata, K.; Ikada, Y. Crosslinking of hyaluronic acid with water-soluble carbodiimide. *J. Biomed. Mater. Res.* **1997**, *37*, 243-251.
5. Everaerts, F.; Torrianni, M.; Hendriks, M.; Feijen, J. Biomechanical properties of carbodiimide crosslinked collagen: influence of the formation of ester crosslinks. *J. Biomed. Mater. Res. Part A* **2008**, *85*, 547-555.
6. Guo, P.; Anderson, J.D.; Bozell, J.J.; Zivanovic, S. The effect of solvent composition on grafting gallic acid onto chitosan via carbodiimide. *Carbohydr. Polym.* **2016**, *140*, 171-180.
7. Piegat, A.; Goszczyńska, A.; Idzik, T.; Niemczyk, A. The importance of reaction conditions on the chemical structure of N, O-acylated chitosan derivatives. *Molecules* **2019**, *24*, 3047.

8. Rivas, B.L.; Pereira, E.; Paredes, J.; Sanchez, J. Removal of arsenate from ionic mixture by anionic exchanger water-soluble polymers combined with ultrafiltration membranes. *Poly. Bull.* **2012**, *69*, 1007-1022.

9. Chen, K.-Y.; Zeng, S.-Y. Preparation and characterization of quaternized chitosan coated alginate microspheres for blue dextran delivery. *Polymers* **2017**, *9,* 210.

10. de Paul Nzuwah Nziko, V.; Shih, J.L.; Jansone-Popova, S.; Bryantsev, V.S. Quantum chemical prediction of pK_a values of cationic ion-exchange groups in polymer electrolyte membranes. *J. Phys. Chem. C* **2018**, *122*, 2490-2501.

11. Karpenko, L.I.; Apartsin, E.K.; Dudko, S.G.; Starostina, E.V.; Kaplina, O.N.; Antonets, D.V.; Volosnikova, E.A.; Zaitsev, B.N.; Bakulina, A.Y.; Venyaminova, A.G.; Ilyichev, A.A.; Bazhan, S.I. Cationic polymers for the delivery of the Ebola DNA vaccine encoding artificial T-cell immunogen. *Vaccines* **2020**, *8*, 718.

12. Chau, M.; Sriskandha, S.E.; Pichugin, D.; Thérien-Aubin, H.; Nykypanchuk, D.; Chauve, G.; Méthot, M.; Bouchard, J.; Gang, O.; Kumacheva, E. Ion-mediated gelation of aqueous suspensions of cellulose nanocrystals. *Biomacromolecules* **2015**, *16*, 2455-2462.

13. Morozova, S.M.; Statsenko, T.G.; Ryabchenko, E.O.; Gevorkian, A.; Adibnia, V.; Lozhkin, M.S.; Kireynov, A.; Kumacheva, E. Multicolored nanocolloidal hydrogel inks. *Adv. Funct. Mater.* **2021**, *31*, 2105470.

14. Wang, X.; Liu, L.; Pu, Q.; Zhu, Z.; Guo, G.; Zhong, H.; Liu, S. Pressure-induced transport of DNA confined in narrow capillary channels. *J. Am. Chem. Soc.* **2012**, *134*, 7400-7405.

15. Dauzenberg, H.; Zintchenko, A. Polycationic graft copolymers as carriers for oligonucleotide delivery. Complex of oligonucleotides with polycationic graft copolymers. *Langmuir* **2001**, *17*, 3096-3102.

16. Wang, C.; Li, X.L Wettig, S.D.; Badea, I.; Foldvari, M.; Verrall, R.E. Investigation of complexes formed by interaction of cationic gemini surfactants with deoxyribonucleic acid. *Phys. Chem. Chem. Phys.* **2007**, *9*, 1616-1628.

17. Roy, K.B.; Antony, T.; Saxena, A.; Bohidar, H.B. Ethanol-induced condensation of calf thymus DNA studied by laser light scattering. *J. Phys. Chem. B* **1999**, 103, 5117-5121.